Fabrication and creep properties of eutectic-composition Al₂O₃/YAG/YSZ sintered composites

F.A. Huamán-Mamani*, C. Jiménez-Holgado** and M. Jiménez-Melendo***

* Departamento de Ciencias Naturales, Universidad Católica San Pablo. Arequipa, Peru

** Department of Chemistry, School of Science, University of Ioannina. 45110 Ioannina, Greece

***Departamento de Física de la Materia Condensada, Universidad de Sevilla. 41080 Sevilla, Spain

***Corresponding author: melendo@us.es

ABSTRACT

Three-phase alumina/YAG/yttria-stabilized cubic zirconia (YSZ) composites were fabricated by a solid-state reaction route starting from commercial powders of Al_2O_3, Y_2O_3 and monoclinic ZrO_2. The final phases Al_2O_3, YAG and YSZ were obtained after calcination of the powder mixtures at 1400 °C. Dense bulk composites were obtained after sintering, with a homogeneous microstructure of fine and equiaxed grains with sizes of 1 μm. Compressive mechanical tests were performed at 1300 – 1450 °C in air at constant load and at constant initial strain rate. A brittle-to-ductile transition was found with increasing temperature. Grain boundary sliding is the main deformation mechanism in the ductile regime, characterized by a stress exponent of 2 and by the absence of dislocation activity and changes in grain morphology. Alumina seems to be the rate-controlling phase owing to the improvement in creep resistance by the presence of yttrium and zirconium of the other two phases.

1. Introduction

Alumina-based composites are probably the most used engineering oxide ceramics nowadays in structural applications, particularly at high temperatures, because of their excellent chemical stability and mechanical properties. Although pure monolithic alumina is inherently brittle, with a low fracture toughness at low and high temperatures [1,2], its mechanical properties can be considerably enhanced by the incorporation of other phases in composite structures, such as fibers, particulates, layers, etc. In particular, particulate composites formed by equiaxed and approximately similar-sized particles exhibit improved thermal and chemical stability relative to their single-phase constituents, thus maintaining optimal mechanical properties of strength, toughness, and thermal shock resistance at elevated temperatures. In this way, dual phase Al_2O_3/ZrO_2 [3–8] and Al_2O_3/YAG [4,9–11] composites have been produced with higher strength, fracture toughness, and creep resistance than their single-phase counterparts. Remarkably, these fine-grained composites exhibit metal-like superplasticity, which contrasts with the premature failure of undoped monolithic alumina owing to the extensive grain growth and cavitation during high-temperature deformation [2,12].

Directionally-solidified alumina-based eutectic ceramics grown from the melt have received much attention in the last years because of their excellent mechanical properties even at temperatures close to the eutectic temperature [13–19], which derive from the special lamellar microstructures obtained during solidification. In particular, directionally-solidified ternary $Al_2O_3/YAG/ZrO_2$ eutectic melts have been shown to have a fracture toughness as high as 8 MPa.m$^{1/2}$ at room temperature [16], and the retention of large flexural, tensile and compressive strengths up to temperatures close to the eutectic temperature [13,14]. The fabrication routes necessary to produce directionally-solidified eutectic ceramics are, however, economically

expensive, no suitable for mass production and impose serious restrictions for obtaining bulk components with custom shapes and sizes. Furthermore, the physical properties of these eutectic ceramics are very anisotropic, depending strongly on the solidification direction. These drawbacks can be mitigated, at least partially, by using sintered particulate composites produced by conventional solid-state reaction routes.

Very few studies are, however, concerned with Al_2O_3/YAG/ZrO_2 (thereinafter AYZ) sintered composites, which have been fabricated with different phase contents: equivolumetric (33 vol%) [20], eutectic-composition [21] and 5 vol% YAG + 5 vol% ZrO_2 particulate-reinforced Al_2O_3 [22]. Precisely on this last material, fabricated by surface modification of the alumina powder with inorganic precursors of the second phases, Palmero et al. [23] have reported the only study addressing the high-temperature mechanical behavior of AYZ sintered ceramics; by means of four-point bending tests from room temperature up to 1500 °C, the authors found an enhanced deformability at temperatures above 1400 °C (though the maximum strain was limited to 4% due to restrictions of the experimental setup). The aim of the present study is therefore two-fold: first, to fabricate and characterize the crystalline phases and microstructure of three-phase AYZ composites with the eutectic composition produced by a conventional ceramic processing route; and second, to investigate their creep response at high temperatures by constant cross-head speed and constant load tests in correlation with microstructural observations, in order to assess the microscopic mechanisms involved in the plastic deformation. The creep of the three-phase composite is compared to that of the single-phase constituents.

2. Experimental procedure

2.1. Starting materials

Samples of polycrystalline AYZ composites with the eutectic composition (65.8 mol% Al_2O_3, 15.6 mol% Y_2O_3, 18.6 mol% monoclinic ZrO_2 [24]) were produced via a conventional solid-state reaction route. Appropriate amounts of high-purity commercial powders ($\geq$ 99.99%, Sigma-Aldrich) of Al_2O_3, Y_2O_3 and monoclinic ZrO_2 were dry ball-milled in agate media for 1 h at 150 rpm using a planetary ball mill (Pulverisette 6, Fritsch, Germany). The resulting powders were calcined at different temperatures between 1200 and 1600 °C in air for 10 h and reground again using the same milling conditions as for the initial mixtures to eliminate possible agglomerates. A calcination temperature as high as 1600 °C was selected because it was reported [25] that the formation of the YAG phase started at 1300 °C in Al_2O_3/Y_2O_3 powder mixtures processed by solid-state reaction, obtaining the single-phase YAG only at temperatures above 1600 °C; below this temperature, the intermediate phases $YAlO_3$ (YAP, orthorhombic perovskite) and $Y_4Al_2O_9$ (YAM, monoclinic) were also present in the mixtures from 1100 to 1400 °C and from 1200 to 1600 °C, respectively. The particle size distribution of the various powder mixtures was analyzed by laser light scattering (Malvern Mastersizer 2000 with distilled water as carrier medium), resulting a number-based median particle size d_{50} of 1.20 μm for the as-received powder, 0.92 μm after the first milling and finally 0.76 μm after calcination and second milling. The calcined powders were analyzed by X-ray diffraction in order to determine the nature and content of the crystalline phases (see below). The powder mixtures were uniaxially pressed at 150 MPa into 20-mm diameter pellets and then isostatically cold pressed at 210 MPa. The resulting green pellets were sintered in air at 1500 °C for 10 h with low heating and cooling rates of 5 °C/min. The bulk density of the composites was determined from weight/dimensions measurements.

2.2. Structural and microstructural characterization

X-ray structure analyses were systematically performed on the calcined AYZ powders as well as in the sintered composites in order to ensure the presence of the required phases. X-ray powder diffractograms were obtained using a Bruker D8 Advance A25 X-ray diffractometer with Cu K$_\alpha$ radiation and Ni filter, equipped with a scintillation detector in $\theta - 2\theta$ Bragg-Bentano configuration (X-ray Laboratory, CITIUS, University of Sevilla, Spain). A continuous scan mode was used to collect 2θ data in the $10 - 120°$ range in steps of $0.015°$ and a scanning speed of 1.8 °/min. Collected X-ray spectra were first processed by the Le Bail method followed by Rietveld refinement using the TOPAS 4.2 Bruker AXS software package to quantify the nature and amount of the different crystalline phases in the powders.

The microstructural characterization of as-sintered and deformed composites was carried out using high-resolution scanning electron microscopy (HRSEM), particularly in back-scattered electron image mode to discern the different crystalline phases, and transmission electron microscopy (TEM) (Microscopy Service, CITIUS, University of Sevilla, Spain). In order to reveal the grain boundaries for SEM observations, sections were cut from the samples and mechanically polished using up to 0.25 μm-grade diamond paste, and then thermally etched at 1300 °C for 2 h in air. The relevant morphological parameters, grain size d (taken as the equivalent planar diameter d = $(4 \times \text{grain area}/\pi)^{1/2}$), form factor F (defined as F = $4\pi \times$ grain area/(grain perimeter)^2) and preferential orientation, were measure by using a semiautomatic image analyzer; over 300 grains were measured for each phase. Thin films for TEM observations were obtained from the as-fabricated and deformed samples following a classical procedure of grinding and ion-thinning until electron transparency of sliced sections. Elemental composition analysis was performed by energy dispersive X-ray spectroscopy (EDS) in both SEM and TEM to characterize the various phases present in the composites. Wavelength dispersive X-ray fluorescence spectroscopy (WDXRF Malvern Pananalytical Axios, Germany, X-Ray Laboratory,

CITIUS, University of Sevilla, Spain) was also used to determine the chemical composition of the sintered composites.

2.3. Mechanical tests

Prismatic specimens of 5 x 3 x 3 mm in size were cut from the sintered pellets and used for mechanical experiments. Two types of compressive tests were carried out in air at temperatures T between 1300 and 1450 °C: (i) under constant load in a creep machine, at nominal stresses σ between 50 and 120 MPa; the raw data, instantaneous specimen length l(t) vs. time t, were plotted as $\log \dot{\varepsilon} - \varepsilon$ curves, where ε is the true strain (= ln(l_o/l(t)), with l_o the initial length) and $\dot{\varepsilon} = d\varepsilon / dt$ is the instantaneous strain rate. And (ii) at constant cross-head speed in an universal testing machine at different initial strain rates $\dot{\varepsilon}_o$; the recorded data, load vs. time, were analyzed in σ - ε curves, where σ and ε are the true stress and the true strain, respectively. After the completion of tests, the specimens were cooled under load to preserve the final microstructure.

The mechanical data were analyzed using the standard high-temperature power law for steady-state deformation [26]:

$$\dot{\varepsilon} = A\sigma^n d^{-p} \exp(-Q / RT) \tag{1}$$

where A is a parameter depending on the deformation mechanism, n is the stress exponent, p is the grain size exponent, Q is the activation energy for creep and R is the gas constant. The parameters n and Q, characteristics of the deformation mechanism, were measured from stress and temperature changes, respectively. The specimens were typically deformed to total strains of 50-60 % (unless premature failure occurred) for subsequent microstructural observations.

3. Results and discussion

3.1. Phase composition of the calcined powders

Figure 1 shows the X-ray diffractograms of the as-milled and calcined powders at temperatures between 1200 and 1600 °C. The patterns are rather complex because up to seven different phases could be identified at intermediate temperatures. Every peak in the diffractograms was indexed according to one of the following PDF-2002 database reference patterns (International Centre for Diffraction Data, ICDD): α-Al_2O_3 (No. 05-0712), Y_2O_3 (No. 89-5591), monoclinic ZrO_2 (No. 36-0420), $Y_4Al_2O_9$ (YAM, No. 34-0368), $YAlO_3$ (YAP, No. 74-1334), $Y_3Al_5O_{12}$ (YAG, No. 33-0040) and $Zr_{0.72}Y_{0.28}O_{1.862}$ (YSZ, No. 77-2112). The volume fractions of the crystalline phases were quantified by Rietveld refinement, and are gathered in Table 1.

In the as-ground powder (Figure 1 and Table 1), the three original phases Al_2O_3, Y_2O_3 and monoclinic ZrO_2 were identified, indicating that no additional phases formed during the milling process. At 1200 °C, seven different phases were detected: Al_2O_3, Y_2O_3, monoclinic and cubic ZrO_2, and the three phases of the Al_2O_3/Y_2O_3 system, YAM, YAP and YAG. YAM and YAP are undesired phases because they exhibit poorer mechanical strengths than YAG. Regarding the zirconia phase, the $Zr_{0.72}Y_{0.28}O_{1.862}$ reference pattern (No. 77-2112) provided the best match to the observed XRD profiles. After Rietveld refinement, a lattice parameter of a = 5.156 ± 0.003 Å was obtained, corresponding to an yttrium composition of 0.27 ± 0.02 at% (equivalent to 15.6 ± 2.0 mol% Y_2O_3 fully-stabilized cubic ZrO_2) according to the Vegard's law [27]. This cubic phase derives from the original low-symmetry monoclinic phase through alloying with substitutional yttrium cations provided by the Y_2O_3 phase. The yttria molar content agrees with the

compositions of 15.5 and 16 mol% Y_2O_3 reported in directionally-solidified AYZ eutectic composites [17] and in 5 vol% ZrO_2 + 5 vol% YAG-reinforced Al_2O_3 sintered composite [22], respectively.

Regarding the evolution of the yttrium aluminate phases, the YAM and YAP phases gradually disappear with increasing the calcination temperature (Figure 1 and Table 1). Single-phase YAG is completely formed at 1400 °C, which is 200 °C lower than the critical temperature reported by Ikesue et al. [25] in the Al_2O_3/Y_2O_3 system. This result suggests that the presence of the zirconia phase inhibits the coarsening of the alumina particles, resulting in faster diffusion processes. Higher calcination temperatures practically do not introduce further phase changes.

The sintered compacts were finely crushed and powdered for further XRD analyses, which were found to be virtually identical to the calcined powders. From Rietveld refinement, the sintered composites consist of 39.1 vol% Al_2O_3, 40.1 vol% YAG and 20.8 vol% YSZ (Table 1), indicating the absence of significant phase evolution during the sintering step. Table 1 also collects the phase contents expected by assuming a complete reaction of the oxide precursor powders as well as the values reported in directionally-solidified AYZ eutectic melts [14] and in eutectic-composition AYZ sintered polycrystals [21] (in this case, the zirconia phase was stabilized in the tetragonal structure due to the use of 3 mol% yttria-stabilized tetragonal zirconia 3YTZP powder as precursor), showing a fair agreement with the present values estimated from XRD spectra.

3.2. Microstructural characterization of the sintered composites

Figure 2 depicts representative SEM and TEM micrographs of the as-sintered composites. Figure 2(a) corresponds to a secondary electron SEM image showing a homogeneous distribution of

fine and equiaxed grains, with very little porosity mainly located at triple grain junctions. YAG

and YSZ phases are hardly distinguishable in this image mode, but they can be easily separated

in backscattered SEM mode, as illustrated in Figure 2(b) (same area than in Figure 2(a)): alumina

is the dark phase, YAG is gray and YSZ is white (the three phases were identified by energy

dispersive X-ray microanalysis).

The average bulk density of the sintered composites is 4530 ± 50 kg/m^3. The theoretical density,

calculated from the expected phase composition (Table 1), is 4600 kg/m^3 (densities of 3990,

4550 and 5840 kg/m^3 were used for alumina, YAG and YSZ, respectively), resulting a relative

density of 98.5%. The porosity level estimated from SEM micrographs was 1.1 ± 0.3%, in

agreement with density measurements. In this regard, we have tried unsuccessfully to fabricate

the composites directly from the compaction and sintering of the original precursor powders

without previous calcination, as made by Oelgardt et al. [21]. Though the expected Al$_2$O$_3$, YAG

and YSZ were the only phases detected in the sintered ceramics, with grain sizes similar to those

found in the composites obtained from the calcined powders, the relative density was as low as

62 ± 2%, compared to densities higher than 90% reported by Oelgardt et al. [21] for the same

temperature and time of sintering. The different behavior may be related to the use of different

initial zirconia powders, 3 mol% yttria-stabilized tetragonal zirconia (3YTZP) in the Oelgardt et

al. study and monoclinic zirconia in the present one, which resulted in ternary composites with

zirconia phases of different crystalline structures (Table 1).

TEM observations of the as-received sintered composites indicated that the grain boundaries

are well facetted, equiaxed and free of secondary grain boundary phases (Figure 2(c)). No

dislocations activity within the grains was observed except for occasional dislocation arrays in

the larger alumina grains (Figure 2(d)). These defects may be originated by the compressive

residual stresses induced on the alumina grains by the thermal expansion mismatch between the different phases (particularly with zirconia [19]) upon solidification from the sintering temperature, along with the inherent thermal expansion-anisotropy of alumina.

The chemical composition of the as-received composites was measured by WDXRF and EDS-SEM and EDS-TEM. The results are compiled in Table 2, showing a good agreement between both techniques. The major impurity is silicon, with an average content of 0.12 wt% (estimated error of 0.05 wt%), due to contamination during the milling process. In this regard, it should be noted that a glassy grain-boundary phase has been observed in 3YTZP with impurity contents above 0.1 wt%, not detected in materials with higher purity [28]. It seems to be the case in the present composites, where no secondary phases are observed either at triple points or along grain boundaries.

The grain size distributions of the three phases are shown in Figure 3. The zirconia phase has the smaller grain size, with an average value d = 0.8 ± 0.6 μm (uncertainty corresponds to the standard deviation of the grain size distribution). The other two phases Al_2O_3 and YAG have very similar grain size distributions, with mean values d = 1.1 ± 0.5 μm and d = 1.0 ± 0.5 μm, respectively. The average form factor of the grains is F = 0.8 ± 0.1 for the three phases, indicating a regular grain growth during sintering, without preferential grain orientation. For the sake of comparison, the microstructure of a directionally-solidified AYZ eutectic composite grown from the melt with an interphase (lamellar) spacing similar to the grain size in the present sintered composites is shown in Figures 2(e) and 2(f). It is formed by a complex three-dimensional network of interpenetrating single crystal phases, without grain boundaries separating the individual phases. The interconnected phases form a Chinese script-like microstructure on transverse sections (Figure 2(e)), which are elongated along the growth direction (Figure 2(f)).

3.3. General creep behavior

Figure 4 displays the true stress σ – true strain ε curves for sintered composites deformed at temperatures between 1300 and 1450 °C in air at an initial strain rate $\dot{\varepsilon}_0 = 2x10^{-5}$ s^{-1}. There is a progressive transition from a brittle-to-ductile behavior with increasing temperature. Below 1300 °C, the composite fractured catastrophically without undergoing any plastic deformation. At 1300 °C, the composite failed after reaching a maximum stress of nearly 600 MPa, with little plastic deformation. On the contrary, at 1400 °C and above, the composites underwent very large plastic deformations, exceeding 50% of strain without signals of macroscopic damage. In this ductile regime, the slopes of the $\sigma - \varepsilon$ curves are rather constant, indicating the attainment of a steady state of deformation (the continuous shortening of specimens during compressive constant cross-head speed tests increases monotonically the instantaneous strain rate with respect to the initial one, leading to a slightly positive slope of the $\sigma - \varepsilon$ curves). At the intermediate temperature of 1350 °C, the composites exhibit a semiductile behavior characterized by a continuous decrease of stress with strain after the yield point, indicating a progressive degradation of the material by creep damage. It is remarkable however that, despite this softening, the composites still retain a relatively high strength (compared to the yield stress) at a true strain as large as 50% without evidence of macroscopic failure. For the sake of comparison, the $\sigma - \varepsilon$ curve for the directionally-solidified AYZ eutectic composite shown in Figures 2(e) and 2(f) and deformed at T = 1400 °C and $\dot{\varepsilon}_0 = 2x10^{-5}$ s^{-1} is also plotted in Figure 4 (dotted curve). The specimen fractured without plastic deformation after reaching a maximum stress of 260 MPa, which lies in between the semibrittle and ductile regions of the sintered composites.

3.4. Microstructure of deformation

The microstructure of the strained samples (Figure 5) correlates well with the mechanical behavior displayed by the corresponding stress – strain curves. At the higher temperatures (ductile regime), the specimens deform homogeneously without noticeable changes in grain morphology (Figures 5(a) and 5(b)); the grain size d, shape F and preferential orientation distributions of the three phases remain identical to those of unstrained specimens. The lack of morphological changes after deformation suggests that grain boundary sliding is the dominant mechanism for steady deformation in this material, with the grains sliding on each other along their boundaries to accommodate the macroscopic deformation. Such a deformation mechanism has been reported widely in fine-grained superplastic metals and ceramics [5–8,28–33]. Palmero et al. [23] also reported a brittle-to-ductile transition in the flexural strength with temperature on a 90 vol% Al_2O_3 + 5 vol% YAG + 5 vol% ZrO_2 sintered composite with average grain sizes of 0.82, 0.45 and 0.28 μm for the three phases, respectively, deformed in four-point bending up to 1500 °C; below 1350 °C, the composite displayed a brittle behavior, changing to an enhanced plasticity above 1450 °C. Despite the limited strain of 4 % attained in this region due to limitations of the experimental setup and the short duration of the tests (20-200 s), the authors also suggested that gran boundary sliding was the mechanism responsible for the improved plasticity. Similarly, Pilling and Payne [34] found an enhanced superplastic behavior (with true strains higher than 120%) in ternary Al_2O_3/3YTZP/Al_2TiO_5 composites with a relative density of 98.5% and average grain size of d = 0.63 μm for the three phases, deformed between 1420 and 1520 °C.

TEM observations performed on 50%-deformed AYZ composites in steady-state conditions (Figure 5(f)) reveal that the grains remained equiaxed and without signs of cavitation along the

boundaries. Though the grains were slightly more stressed that in the undeformed state, the structure and density of dislocations were similar to those found in the unstrained specimens: the YAG and zirconia grains remained free of dislocations, and only in the larger alumina grains some dislocations could be observed. These observations suggest that dislocations do not play an important role in the steady-state plastic deformation of the three-phase AYZ sintered composites.

As the temperature decreases, the local stresses generated during the grain boundary sliding can no longer be fully relaxed, and microcavities appear along the grain boundaries and triple points, as shown in Figures 5(c) and 5(d) for a composite deformed up to 50% in the semibrittle region. These cavities, however, did not grow and coalesce into cracks despite the large strains attained, resulting in a creep damage-tolerant regime. Finally, as the deformation conditions become more severe, the microcavities coalesce leading to the failure of the specimen. SEM observations of these fracture surfaces (Figure 5(e)) show the presence of multiple microcracks distributed over the volume of the sample, indicating the occurrence of significant crack deflection along grain boundaries, which is at the origin of the creep damage-tolerant regime. The fracture mode was mainly intragranular in the alumina phase and intergranular in the YAG and YSZ phases. It has been reported that the high-temperature fracture mode of pure alumina is intergranular, changing to intragranular upon the addition of dopants because of the chemical alteration of the grain boundaries by cation segregation [1,35,36]. Such an effect is likely to occur in the present composites due to the presence of zirconium and yttrium cations provided by the YSZ and YAG phases.

3.5. Steady-state creep parameters

3.5.1. Stress exponent n

In order to corroborate that grain boundary sliding is the main deformation mechanism operating in the composites in steady-state conditions, creep tests at constant load were performed to evaluate the stress exponent n of the creep equation (Eq. 1), which characterize the deformation mechanism [26,29]. Figure 6(a) shows a representative $\log \dot{\varepsilon} - \varepsilon$ curve obtained at 1400 °C with several determinations of n by up- and down-load changes (differential method) between 100 and 120 MPa. In this kind of plots, the steady states are characterized by a constant negative slope because of the increase in specimen section during testing. An average stress exponent of n = 1.9 ± 0.1 was estimated from the load changes, which is very close to the value of 2 reported for superplastic materials where grain boundary sliding is the dominant mechanism of deformation [7,8,28–30,32,33]. With regard to the creep curve in Figure 6(a), several additional points should be noted. First, the strain rate levels are maintained after positive and negative load changes, indicating that no significant microstructural changes took place during testing, in agreement with SEM observations. Second, it can be easily shown from Eq. (1) that the slope α of the $\log \dot{\varepsilon} - \varepsilon$ curve is equal to -n in the case of homogeneous deformation (i.e., when no grain coarsening, cavitation or other flaws occur during testing); an experimental value of α = -2.1 was found, very close to the value of n measured by load changes. Third, the mechanical behavior of the composite is identical regardless of whether testing is at constant initial strain rate or at constant load. For instance, extrapolating in Figure 6(a) the strain rate to ε = 0 (to eliminate the effect of the increase in specimen section with strain), a value of $\dot{\varepsilon}_o \simeq 2 \text{x} 10^{-5} \text{ s}^{-1}$ is found at 120 MPa and 1400 °C, identical to the value found at constant strain rate for the same experimental conditions (Figure 4). And fourth, the steady-state stages are reached almost immediately (within a strain < 2%) upon up- and down-load changes (Figure 6(a)), indicating again that the plastic flow of the composites is not related with a dislocation

recovery-controlled creep mechanism, which needs the establishment or the modification of a dislocation substructure prior to the attainment of the steady state. These features highlight the large deformability of the AYZ composites, based on the superior microstructural stability of the phases.

As noted above, a value of n = 2 has been systematically reported in fine-grained metals and ceramics [7,8,28–30,32,33], where grain boundary sliding is the dominant deformation mechanism. This is also the value predicted by most theoretical and semiphenomenological models developed to explain the superplastic behavior of fine-grained materials [29]. The set of experimental results found in the present work: a stress exponent close to 2, extended steady states of deformation, absence of changes in grain size and morphology after large strains and the absence of dislocation substructures and creep transients, allow to conclude that the creep of the three-phase AYZ sintered composites takes place by grain boundary sliding.

3.5.2. Activation energy Q

For grain boundary sliding, the steady-state deformation is usually controlled by the diffusion necessary to accommodate the local stresses generated during sliding. The creep activation energy Q (Eq. (1)) can be thus identified with the diffusion energy of the slowest moving species in the material along the faster path. Q has been measured by up- and down-temperature changes during steady-state creep, as illustrated in Figure 6(b) for changes between 1400 and 1450 $^\circ$C at a fixed initial stress of 103 MPa. An average value of Q = 680 ± 50 kJ/mol was found, which is substantially higher than the creep energies reported for the single-phase constituents: 400-500 kJ/mol in Al_2O_3 [4,33,37,38], 430-520 kJ/mol in YSZ [4,28,39] and 530-580 kJ/mol in YAG [4,40]. These creep energies are consistent, though with some scatter, with the values reported

for cation diffusion (the slowest moving ionic species) in cubic zirconia [28,41] and YAG [40]. The mechanisms of diffusion in alumina are however still uncertain [42–44] due to its highly extrinsic character and also because the diffusion energies along grain boundaries are substantially higher than in volume, contrary to what is generally found in other materials. Despite the scatter, it must be noted that oxygen diffuses several orders of magnitude faster than aluminum both in bulk and along (sub)grain boundaries when measured on the same suite of crystals [45–47], thus becoming the rate-limiting species in alumina. For the sake of clarity, Table 3 compiles the creep and the corresponding diffusion energies for the single-phase monoliths, along with creep energies for binary alumina/zirconia [4] and alumina/YAG [4,48] composites.

3.6. Strain rate-controlling phase in the AYZ composite

This discrepancy between the creep energies of the AYZ composite Q = 680 kJ/mol and the single-phase constituents is also encountered when comparing their strain rates. Figure 7 shows the variation of the grain size-compensated strain rate with stress at 1400 $^\circ$C for the AYZ composite (black solid line) and the monolithic counterparts (slashed areas). Strain rates have been normalized with a grain size exponent p = 2 in Eq. (1), intermediate between the values of 1 and 3 reported for grain boundary sliding [7,10,28,29,33,37] (in fact, the discussion is not affected by the choice of p due to the small range of grain sizes involved). It can be seen that the strain rates of the single-phase monoliths are similar among them, but higher than that of the AYZ composite. This unexpected result has been also reported in binary Al_2O_3/YAG [4,48] and Al_2O_3/ZrO_2 composites [4] (AY and AZ, respectively, in Figure 7).

The discrepancy can be understood based on the highly extrinsic character exhibited by alumina noted previously; even a few ppm of impurities/dopants can change drastically the strain rate

because of the hindering of the diffusion processes. It has been reported a decrease by one order of magnitude in the strain rate of Zr-doped alumina with respect to undoped alumina [33,37], and by two orders of magnitude when doped with Y [4,31,37] (Figure 7); the reduction was even more drastic, by a factor of 400, when doubly doped with yttrium and zirconium [31]. Such a behavior has been related to the segregation of dopant cations along the alumina grain boundaries, which restrains the diffusion processes along this path and then retards the creep rate. Cation segregation at grain boundaries has been reported in different ceramic oxides such as yttrium-stabilized zirconia [28], yttrium-doped barium zirconate [30] and other perovskite oxides for solid oxide fuel cells [49]. The intergranular fracture mode of the alumina grains noted above in the brittle region is most likely to occur by the same effect.

Furthermore, the enhanced creep resistance exhibited by cation-doped monolithic Al_2O_3 relative to undoped alumina was systematically accompanied by a significant increase in the creep energy, raising from $Q = 400 - 500$ kJ/mol in nominally pure alumina up to $700 - 800$ kJ/mol in Y- and Zr-doped alumina [4,33,37,38] (Table 3). A similar increase in Q was reported in binary alumina/zirconia and alumina/YAG composites relative to the monolithic constituents (Table 3). The self-diffusion activation energy of oxygen measured in pristine and yttrium-doped alumina also follow the same trend observed in creep (Table 3).

Based on the previous results, it is reasonable to assume that the creep behavior of the alumina phase in the three-phase AYZ composite is modified by the presence of the yttrium and zirconium ions provided by the other two phases, which most likely segregated to the alumina grain boundaries during the sintering step. The load transfer between grains can be now modelled by the isostrain condition (the harder phase controls the overall strain rate) [4,9,12] if the three phases are coupled in the composite, as expected for particulate interpenetrated

phases. In this case, the strain and strain rate are the same for each phase, and the composite (applied) stress σ is given by $\sigma = \sum f_i \sigma_i$ (i = Al$_2$O$_3$, YAG, YSZ), where f_i and σ_i are the volume fraction and stress supported for each phase. Assuming that alumina is the rate-controlling phase in the composite, which is present with a volume fraction of f = 39.1% (Table 1), the model predicts that this phase would carry a stress of σ/f $\cong$ 2.6σ, equivalent to a creep rate of (1/f)^n $\cong$ 7 (with n = 2, the stress exponent) times lower than that of the composite (shown by a black dotted lined in Figure 7). The model predicts thus a reduction of the alumina strain rate by at least a factor of 200 compared to undoped alumina (Figure 7), in close agreement with the behavior reported for yttrium- and zirconium-doped alumina. This result, along with the change in fracture mode and the restrained grain growth of the alumina phase in the composite with respect to undoped monolithic alumina [50], suggests that alumina is strongly influenced by the presence of the cations of the other two phases, changing the nature and properties of their grain boundaries. Furthermore, the present results indicate that Al$_2$O$_3$/Y$_3$Al$_5$O$_{12}$/YSZ sintered composites could compete with melt-growth eutectic analogs by tailoring the microstructure through the control of the processing parameters to achieve the desired properties.

4. Conclusions

Al$_2$O$_3$/YAG/cubic ZrO$_2$ sintered composites with the ternary eutectic composition have been successfully fabricated by solid-state reaction. Starting with Al$_2$O$_3$, Y$_2$O$_3$ and monoclinic zirconia powders as precursors, X-ray diffraction analysis indicates that the final phases of Al$_2$O$_3$, YAG and Y$_2$O$_3$ fully-stabilized cubic zirconia, without other intermediate phases, are obtained at a calcination temperature of 1400 °C. Bulk composites with a relative density of 98.5% were obtained after sintering at 1500 °C in air for 10 h. The volume fractions measured for each phase are consistent with the values found in melt-growth AYZ eutectic composites. The

microstructure is formed by a homogeneous distribution of equiaxed and fine grains with average sizes of 1 μm for the three phases.

Compressive mechanical tests were performed at constant cross-head speed and at a constant load in air at 1300 – 1450 °C. A gradual brittle-ductile transition occurs when the temperature increases. In the ductile region, extended steady states of deformation are attained without signals of macroscopic failure. In this regime, the shape and size of the grains remain unaffected by the deformation process, even after strains larger than 50%. The stress exponent n measured in this region is nearly 2, as found in fine-grained superplastic metals and ceramics. These results, together with the absence of dislocation activity in the grains and creep transitories, suggest that grain boundary sliding is the main deformation mechanism in steady-state conditions. As the temperature decreases, the local stresses generated during grain sliding are no longer fully accommodated, and microcavitation takes place along grain boundaries; however, the combination of elevated plasticity and great ability to withstand such flaws resulted in a creep damage-tolerant regime. Eventually, the microcavities coalesce into microcracks leading to the final failure of the composite. The comparison with the monolithic counterparts suggests that the creep rate of the composite is primarily controlled by the alumina phase, which is strongly influenced by the presence of the zirconium and yttrium cations of the other two phases.

References

[1]   A.G. Robertson, D.S. Wilkinson, C.H. Caceres, Creep and Creep Fracture in Hot-Pressed Alumina, J. Am. Ceram. Soc. 74 (1991) 915–921. https://doi.org/10.1111/j.1151-2916.1991.tb04322.x.

[2]   D.S. Wilkinson, C.H. Caceres, A.G. Robertson, Damage and Fracture Mechanisms During High-Temperature Creep in Hot-Pressed Alumina, J. Am. Ceram. Soc. 74 (1991) 922–933. https://doi.org/10.1111/j.1151-2916.1991.tb04323.x.

[3]   J.D. French, H.M. Chan, M.P. Harmer, G.A. Miller, High-Temperature Fracture Toughness of Duplex Microstructures, J. Am. Ceram. Soc. 79 (1996) 58–64. https://doi.org/10.1111/j.1151-2916.1996.tb07880.x.

[4]   J.D. French, J. Zhao, M.P. Harmer, H.M. Chan, G.A. Miller, Creep of Duplex Microstructures, J. Am. Ceram. Soc. 77 (1994) 2857–2865. https://doi.org/10.1111/j.1151-2916.1994.tb04515.x.

[5]   D.M. Owen, A.H. Chokshi, The constant stress tensile creep behaviour of a superplastic zirconia-alumina composite, J. Mater. Sci. 29 (1994) 5467–5474. https://doi.org/10.1007/BF01171563.

[6]   M. Jiménez-Melendo, C. Clauss, A. Domínguez-Rodríguez, G. De Portu, E. Roncari, P. Pinasco, High temperature plastic deformation of multilayered YTZP/ZTA composites obtained by tape casting, Acta Mater. 46 (1998) 3995–4004. https://doi.org/10.1016/S1359-6454(98)00066-4.

[7]   L. Clarisse, R. Baddi, A. Bataille, J. Crampon, R. Duclos, J. Vicens, Superplastic deformation mechanisms during creep of alumina-zirconia composites, Acta Mater. 45 (1997) 3843–3853. https://doi.org/10.1016/S1359-6454(97)89771-6.

[8]   F. WAKAI, H. KATO, Superplasticity of TZP/AI2O3 Composite, Adv. Ceram. Mater. 3 (1988)

71–76. https://doi.org/10.1111/j.1551-2916.1988.tb00173.x.

[9]   H. Duong, J. Wolfenstine, Creep behavior of fine-grained two-phase Al2O3Y3Al5O12 materials, Mater. Sci. Eng. A. 172 (1993) 173–179. https://doi.org/10.1016/0921-5093(93)90438-K.

[10]   L.N. Satapathy, A.H. Chokshi, Microstructural development and creep deformation in an alumina-5% yttrium aluminum garnet composite, J. Am. Ceram. Soc. 88 (2005) 2848–2854. https://doi.org/10.1111/j.1551-2916.2005.00307.x.

[11]   H. Wang, L. Gao, Z. Shen, M. Nygren, Mechanical properties and microstructures of A12O3-5 vol% YAG composites, J. Eur. Ceram. Soc. 21 (2001) 779–783. https://doi.org/10.1016/S0955-2219(00)00262-4.

[12]   A. Morales-Rodríguez, A. Domínguez-Rodríguez, G. de Portu, M. Jiménez-Melendo, Creep mechanisms of laminated alumina/zirconia-toughened alumina composites, J. Eur. Ceram. Soc. 29 (2009) 1625–1630. https://doi.org/10.1016/j.jeurceramsoc.2008.09.017.

[13]   J.H. Lee, A. Yoshikawa, Y. Murayama, Y. Waku, S. Hanada, T. Fukuda, Microstructure and mechanical properties of Al2 O3/Y3Al5O12/ZrO2 ternary eutectic materials, J. Eur. Ceram. Soc. 25 (2005) 1411–1417. https://doi.org/10.1016/j.jeurceramsoc.2005.01.034.

[14]   J.I. Peña, M. Larsson, R.I. Merino, I. de Francisco, V.M. Orera, J. LLorca, J.Y. Pastor, A. Martín, J. Segurado, Processing, microstructure and mechanical properties of directionally-solidified Al2O3-Y3Al5O12-ZrO2 ternary eutectics, J. Eur. Ceram. Soc. 26 (2006) 3113–3121. https://doi.org/10.1016/j.jeurceramsoc.2005.11.005.

[15]   F.A. Huamán-Mamani, M. Jiménez-Melendo, M.C. Mesa, P.B. Oliete, Microstructure and high-temperature mechanical behavior of melt-growth Al 2O 3/Er 3Al 5O 12/ZrO 2 ternary eutectic composites, in: J. Alloys Compd., Elsevier, 2012: pp. S527–S531. https://doi.org/10.1016/j.jallcom.2012.01.105.

[16]   J. Zhang, H. Su, K. Song, L. Liu, H. Fu, Microstructure, growth mechanism and mechanical

property of Al2O3-based eutectic ceramic in situ composites, J. Eur. Ceram. Soc. 31 (2011) 1191–1198. https://doi.org/10.1016/j.jeurceramsoc.2010.11.008.

[17]   L. Mazerolles, N. Piquet, M.F. Trichet, L. Perrière, D. Boivin, M. Parlier, New microstructures in ceramic materials from the melt for high temperature applications, Aerosp. Sci. Technol. 12 (2008) 499–505. https://doi.org/10.1016/j.ast.2007.12.002.

[18]   S. Wang, J. Liu, Microstructure and growth characteristics of Al2O3/Er2O3/ZrO2 solidified ceramics with different compositions, J. Eur. Ceram. Soc. 41 (2021) 4284–4293. https://doi.org/10.1016/j.jeurceramsoc.2021.01.058.

[19]   J.Y. Pastor, A. Martín, J.M. Molina-Aldareguía, J. LLorca, P.B. Oliete, A. Larrea, J.I. Peña, V.M. Orera, R. Arenal, Superplastic deformation of directionally solidified nanofibrillar Al2O3-Y3Al5O12-Zr O2 eutectics, J. Eur. Ceram. Soc. 33 (2013) 2579–2586. https://doi.org/10.1016/j.jeurceramsoc.2013.03.033.

[20]   D.K. Kim, W.M. Kriven, Processing and characterization of multiphase ceramic composites part II: Triplex composites with a wide sintering temperature Range, in: J. Am. Ceram. Soc., John Wiley & Sons, Ltd, 2008: pp. 793–798. https://doi.org/10.1111/j.1551-2916.2008.02262.x.

[21]   C. Oelgardt, J. Anderson, J.G. Heinrich, G.L. Messing, Sintering, microstructure and mechanical properties of Al2O3-Y2O3-ZrO2 (AYZ) eutectic composition ceramic microcomposites, J. Eur. Ceram. Soc. 30 (2010) 649–656. https://doi.org/10.1016/j.jeurceramsoc.2009.09.011.

[22]   P. Palmero, A. Sola, V. Naglieri, D. Bellucci, M. Lombardi, V. Cannillo, Elaboration and mechanical characterization of multi-phase alumina-based ultra-fine composites, J. Mater. Sci. 47 (2012) 1077–1084. https://doi.org/10.1007/s10853-011-5898-5.

[23]   P. Palmero, G. Pulci, F. Marra, T. Valente, L. Montanaro, Al2O3/ZrO2/Y3Al5O12 Composites: A High-Temperature Mechanical Characterization, Materials (Basel). 8

(2015) 611–624. https://doi.org/10.3390/ma8020611.

[24] S.N. Lakiza, L.M. Lopato, L. V. Nazarenko, Z.A. Zaitseva, The liquidus surface in the Al2O3-ZrO2-Y2O3 phase diagram, Powder Metall. Met. Ceram. 33 (1995) 595–598. https://doi.org/10.1007/BF00559667.

[25] A. Ikesue, T. Kinoshita, K. Kamata, K. Yoshida, Fabrication and Optical Properties of High-Performance Polycrystalline Nd:YAG Ceramics for Solid-State Lasers, J. Am. Ceram. Soc. 78 (1995) 1033–1040. https://doi.org/10.1111/j.1151-2916.1995.tb08433.x.

[26] J.-P. Poirier, Creep of Crystals, Cambridge University Press, 1985. https://doi.org/10.1017/CBO9780511564451.

[27] M. Yashima, N. Ishizawa, M. Yoshimura, Application of an Ion-Packing Model Based on Defect Clusters to Zirconia Solid Solutions: II, Applicability of Vegard's Law, J. Am. Ceram. Soc. 75 (1992) 1550–1557. https://doi.org/10.1111/j.1151-2916.1992.tb04223.x.

[28] M. Jiménez-Melendo, A. Domínguez-Rodríguez, A. Bravo-León, Superplastic flow of fine-grained yttria-stabilized zirconia polycrystals: Constitutive equation and deformation mechanisms, J. Am. Ceram. Soc. 81 (1998) 2761–2776. https://doi.org/10.1111/j.1151-2916.1998.tb02695.x.

[29] T.G. Nieh, J. Wadsworth, O.D. Sherby, Superplasticity in Metals and Ceramics, Cambridge University Press, 1997. https://doi.org/10.1017/CBO9780511525230.

[30] D. Ciria, M. Jiménez-Melendo, V. Aubin, G. Dezanneau, High-temperature mechanical behavior of proton-conducting yttrium-doped barium zirconate perovskite, J. Eur. Ceram. Soc. 41 (2021) 1374–1383. https://doi.org/10.1016/j.jeurceramsoc.2020.09.069.

[31] S. Yasuda, H. Yoshida, T. Yamamoto, T. Sakuma, Improvement of High-temperature Creep Resistance in Polycrystalline Al<SUB>2</SUB>O<SUB>3</SUB> by Cations Co-doping, Mater. Trans. 45 (2004) 2078–2082. https://doi.org/10.2320/matertrans.45.2078.

[32]   F. WAKAI, S. SAKAGUCHI, Y. MATSUNO, Superplasticity of Yttria-Stabilized Tetragonal ZrO2 Polycrystals, Adv. Ceram. Mater. 1 (1986) 259–263. https://doi.org/10.1111/j.1551-2916.1986.tb00026.x.

[33]   F. Wakai, T. Nagano, T. Iga, Hardening in creep of alumina by zirconium segregation at the grain boundary, J. Am. Ceram. Soc. 80 (1997) 2361–2366. https://doi.org/10.1111/j.1151-2916.1997.tb03128.x.

[34]   J. Pilling, J. Payne, Superplasticity in Al2O3▯ZrO2▯Al2TiO5 ceramics, Scr. Metall. Mater. 32 (1995) 1091–1097. https://doi.org/10.1016/0956-716X(94)00007-5.

[35]   R.F. COOK, A.G. SCHROTT, Calcium Segregation to Grain Boundaries in Alumina, J. Am. Ceram. Soc. 71 (1988) 50–58. https://doi.org/10.1111/j.1151-2916.1988.tb05759.x.

[36]   G.D. West, J.M. Perkins, M.H. Lewis, The effect of rare earth dopants on grain boundary cohesion in alumina, J. Eur. Ceram. Soc. 27 (2007) 1913–1918. https://doi.org/10.1016/j.jeurceramsoc.2006.07.001.

[37]   J. Cho, C.M. Wang, H.M. Chan, J.M. Rickman, M.P. Harmer, Role of segregating dopants on the improved creep resistance of aluminum oxide, Acta Mater. 47 (1999) 4197–4207. https://doi.org/10.1016/S1359-6454(99)00278-5.

[38]   H. Yoshida, Y. Ikuhara, T. Sakuma, High-temperature creep resistance in rare-earth-doped, fine-grained Al2O3, J. Mater. Res. 13 (1998) 2597–2601. https://doi.org/10.1557/JMR.1998.0362.

[39]   B. Sudhir, A.H. Chokshi, Compression Creep Characteristics of 8-mol%-Yttria-Stabilized Cubic-Zirconia, J. Am. Ceram. Soc. 84 (2001) 2625–2632. https://doi.org/10.1111/j.1151-2916.2001.tb01063.x.

[40]   M. Jiménez-Melendo, H. Haneda, H. Nozawa, Ytterbium Cation Diffusion in Yttrium Aluminum Garnet (YAG) - Implications for Creep Mechanisms, J. Am. Ceram. Soc. 84 (2001) 2356–2360. https://doi.org/10.1111/j.1151-2916.2001.tb01014.x.

[41] M. Kilo, M.A. Taylor, C. Argirusis, G. Borchardt, B. Lesage, S. Weber, S. Scherrer, H. Scherrer, M. Schroeder, M. Martin, Cation self-diffusion of 44Ca, 88Y, and 96Zr in single-crystalline calcia- and yttria-doped zirconia, J. Appl. Phys. 94 (2003) 7547–7552. https://doi.org/10.1063/1.1628379.

[42] A.H. Heuer, Oxygen and aluminum diffusion in α-Al2O3: How much do we really understand?, J. Eur. Ceram. Soc. 28 (2008) 1495–1507. https://doi.org/10.1016/j.jeurceramsoc.2007.12.020.

[43] J.H. Harding, K.J.W. Atkinson, R.W. Grimes, Experiment and theory of diffusion in alumina, in: J. Am. Ceram. Soc., American Ceramic Society, 2003: pp. 554–59. https://doi.org/10.1111/j.1151-2916.2003.tb03340.x.

[44] J. Pelleg, Diffusion in Ceramics, Springer International Publishing, Cham, 2016. https://doi.org/10.1007/978-3-319-18437-1.

[45] D. Prot, M. Le Gall, B. Lesage, A.M. Huntz, C. Monty, Self-diffusion in α-Al2O3 IV. Oxygen grain-boundary self-diffusion in undoped and yttria-doped alumina polycrystals, Philos. Mag. A Phys. Condens. Matter, Struct. Defects Mech. Prop. 73 (1996) 935–949. https://doi.org/10.1080/01418619608243697.

[46] P. Fielitz, G. Borchardt, S. Ganschow, R. Bertram, A. Markwitz, 26Al tracer diffusion in titanium doped single crystalline α-Al2O3, Solid State Ionics. 179 (2008) 373–379. https://doi.org/10.1016/J.SSI.2008.03.007.

[47] P. Fielitz, G. Borchardt, S. Ganschow, R. Bertram, 26Al Tracer Diffusion in Nominally Undoped Single Crystalline α-Al2O3, Defect Diffus. Forum. 323–325 (2012) 75–79. https://doi.org/10.4028/WWW.SCIENTIFIC.NET/DDF.323-325.75.

[48] Y. Waku, N. Nakagawa, H. Ohtsubo, A. Mitani, K. Shimizu, Fracture and deformation behaviour of melt growth composites at very high temperatures, J. Mater. Sci. 36 (2001) 1585–1594. https://doi.org/10.1023/A:1017519113164.

[49]   H.I. Yoon, D.K. Lee, H. Bin Bae, G.Y. Jo, H.S. Chung, J.G. Kim, S.J.L. Kang, S.Y. Chung, Probing dopant segregation in distinct cation sites at perovskite oxide polycrystal interfaces, Nat. Commun. 8 (2017) 1–8. https://doi.org/10.1038/s41467-017-01134-x.

[50]   A. Altay, M.A. Gülgün, Microstructural evolution of calcium-doped α-alumina, in: J. Am. Ceram. Soc., American Ceramic Society, 2003: pp. 623–29. https://doi.org/10.1111/j.1151-2916.2003.tb03349.x.

[51]   T. Nakagawa, I. Sakaguchi, N. Shibata, K. Matsunaga, T. Mizoguchi, T. Yamamoto, H. Haneda, Y. Ikuhara, Yttrium doping effect on oxygen grain boundary diffusion in α-Al2O3, Acta Mater. 55 (2007) 6627–6633. https://doi.org/10.1016/j.actamat.2007.08.016.

[52]   L.A. Xue, X. Wu, I.-W. Chen, Superplastic Alumina Ceramics with Grain Growth Inhibitors, J. Am. Ceram. Soc. 74 (1991) 842–845. https://doi.org/10.1111/j.1151-2916.1991.tb06935.x.

[53]   A.A. Sharif, M.L. Mecartney, Superplasticity in cubic yttria-stabilized zirconia with intergranular silica, Acta Mater. 51 (2003) 1633–1639. https://doi.org/10.1016/S1359-6454(02)00564-5.

TABLE CAPTION

Table 1. Volume fractions (in %) of the crystalline phases present in as-ground and calcined powders as a function of the calcination temperature, and in sintered composites. The expected contents assuming a complete reaction of the initial powders are also shown, as well as the values reported in melt-growth directionally-solidified AYZ eutectic composites (DSE) [14] and in AYZ (with tetragonal zirconia phase) sintered polycrystals [21].

Table 2. Elemental chemical composition of as-sintered AYZ composites measured by wavelength dispersive X-ray fluorescence (WDXRF) and energy dispersive X-ray (EDS) spectroscopies.

Table 3. Activation energies (in kJ/mol) for creep and diffusion (slowest moving species) for the single-phase constituents of the AYZ composite. In alumina, the actual value of Q depends critically on the impurity/dopant level because of its highly extrinsic character. Creep data for binary alumina/YSZ and alumina/YAG composites are also shown.

vol%		α-Al$_2$O$_3$	Y$_2$O$_3$	ZrO$_2$ (monocl.)	Y$_4$Al$_2$O$_9$ (YAM)	YAlO$_3$ (YAP)	Y$_3$Al$_5$O$_{12}$ (YAG)	ZrO$_2$ (15.6 mol% Y$_2$O$_3$)
Powder (this work)	As-ground	60.6	25.2	14.2	-	-	-	-
	1200 ºC	52.3	8.4	13.8	8.9	5.4	5.5	5.7
	1300 ºC	40.7	2.0	13.3	5.0	4.2	28.5	6.3
	1400 ºC	36.5	-	4.5	-	-	42.2	16.8
	1500 ºC	38.0	-	-	-	-	40.3	21.7
	1600 ºC	38.6	-	-	-	-	39.5	21.9
Polycrystal (this work)		39.1					40.1	20.8
Expected		41.2					39.1	19.7
DSE [14]		40					42	18
Polycrystal [21]		45					38	17 (3 mol% Y$_2$O$_3$)

Table 1

wt%	Al	Zr	Hf	Y	Si	Cu	K	Cl	O
WDXRF	30.07	12.30	0.35	20.10	0.12	0.06	0.03	0.05	36.84
EDS	29.2	11.8	0.2	21.3	0.2	-	-	-	37.4

Table 2

Material	Creep	Diffusion
Alumina	453 (undoped) → 698 (Y-doped) [4] 520 (undoped) → 670 - 760 (Zr-doped) [33] 483 (undoped) → 685 (Y-doped), 700 (Zr-doped) [37] 410 (undoped) → 830 (Y-doped) [38]	Oxygen, grain boundary diffusion: 627 (undoped) → 729 (Y-doped) [51] Oxygen, volume diffusion: 567 [51]
YSZ (yttria-stabilized cubic zirconia)	430 - 515 [4,28,39]	Cation, volume diffusion: 400 - 510 [28,41]
YAG	530 - 585 [4,40]	Cation, volume diffusion: 565 [40]
Alumina/ZTA laminates (isostrain configuration)	710 [12]	
Alumina/YSZ (particulates)	633 [4]	
Alumina/YAG(particulates)	670 - 695 [4,40]	
Alumina/YAG (melt growth)	730 [48]	
Three-phase AYZ composite (this work)	680 ± 50	

Table 3

FIGURE CAPTIONS

Figure 1. X-ray diffractograms of Al_2O_3, Y_2O_3 and monoclinic ZrO_2 powder mixtures after milling and calcination at temperatures between 1200 and 1600 °C for 10 h in air. Bragg reflections were indexed according to the PDF-2002 reference patterns (International Centre for Diffraction Data, ICDD) as shown in the top of the figure.

Figure 2. Microstructure of AYZ sintered composites: (a) secondary electron SEM micrograph; (b) backscattered electron SEM micrograph of the same area showing the three phases: Al_2O_3 (dark), YAG (gray) and cubic ZrO_2 (white); (c) and (d) TEM micrographs showing the absence of secondary phases along grain boundaries and the presence of occasional dislocation arrays in the larger alumina grains. For the sake of comparison, the microstructure of a melt-growth AYZ eutectic composite with an interphase spacing similar to the grain size in the sintered composite is also shown: (e) transverse and (f) longitudinal cross-sections relative to the solidification direction (same color contrasts than in (b)).

Figure 3. Grain size distributions of the Al_2O_3, YAG and yttria fully-stabilized cubic ZrO_2 (YSZ) phases in eutectic-composition AYZ sintered composites.

Figure 4. True stress - true strain curves for AYZ sintered composites deformed at an initial strain rate of $\dot{\varepsilon}_0$ = $2x10^{-5}\,s^{-1}$ as a function of temperature. The $\sigma - \varepsilon$ curve for the directionally-solidified AYZ composite (DSE, dashed curve) of Figure 2 deformed at 1400 °C is also shown for comparison.

Figure 5. Microstructure of deformation of AYZ sintered composites: (a) secondary and (b) backscattered electron SEM micrographs of the same area of a specimen 50%-strained in the ductile region at 1400 °C; (c) and (d) same as before for a specimen 50%-strained in the semibrittle region at 1350 °C; (e) fracture surface of a specimen failed at 1300 °C; and (f) TEM image of a sample 50%-deformed in steady-state conditions at 1400 °C. Loading direction is indicated by arrows.

Figure 6. Creep curves plotted as $\log \dot{\varepsilon} - \varepsilon$ for AYZ sintered composites deformed in steady state. Several determinations of (a) the stress exponent n and (b) the activation energy for creep Q (Eq. 1) by stress and temperature changes, respectively, are shown.

Figure 7. Grain size-compensated strain rate against stress at 1400 °C for the three-phase AYZ sintered composite (solid black line). The average behavior of alumina (d = 3.0 μm [4], 1.1 μm [33], 0.5 μm [52]), YAG (1.7 μm [4], 1.7 – 5.3 μm [40]) and cubic zirconia (1.8 μm [4], 3.0 μm [53]) monoliths (dashed areas) is shown, along with data for alumina doped with 10^3 ppm Y^{3+} (2.6 μm [4], 2.2 μm [37]) and with 10^3 ppm Zr^{4+} (0.7 μm [33], 1.7 μm [37]), and for binary alumina/zirconia (AZ) (2.3 μm [4]) and alumina/YAG (AY) (2.0 μm [4], 4.0 μm [48]) composites. The strain rate of the alumina phase (volume fraction of 39.1 vol%) predicted by the isostrain model to explain the overall creep rate of the AYZ composite is also shown (dotted black line).
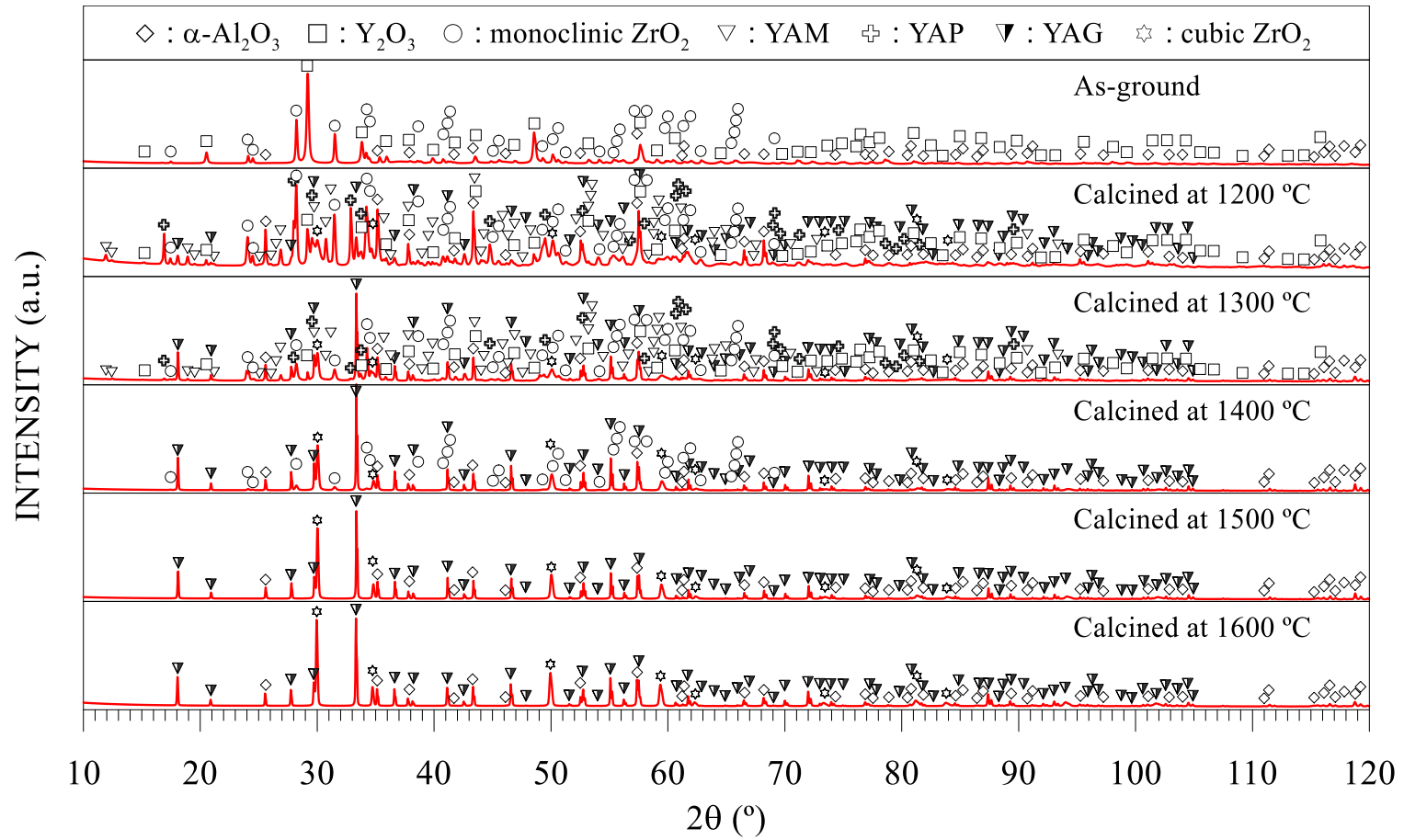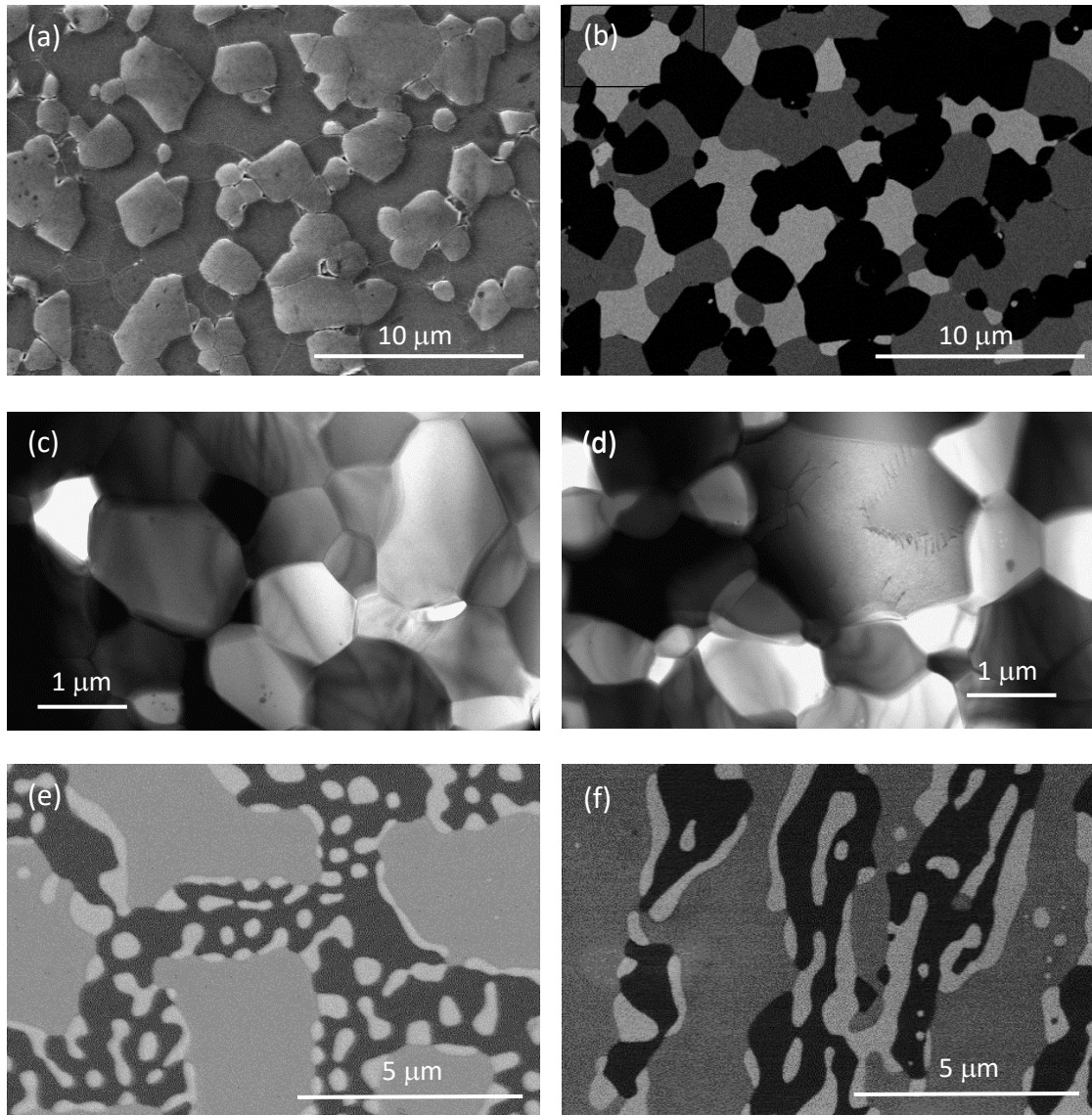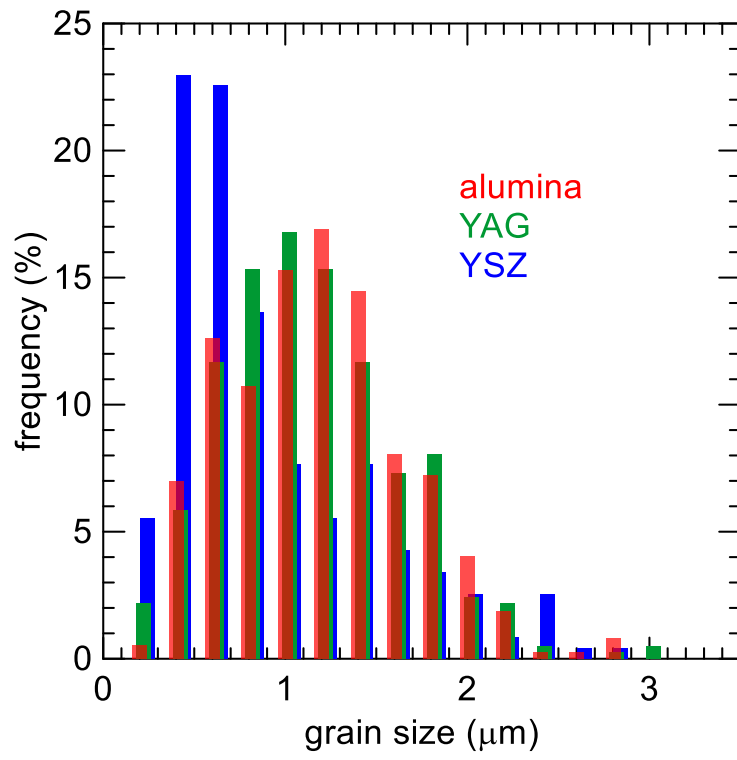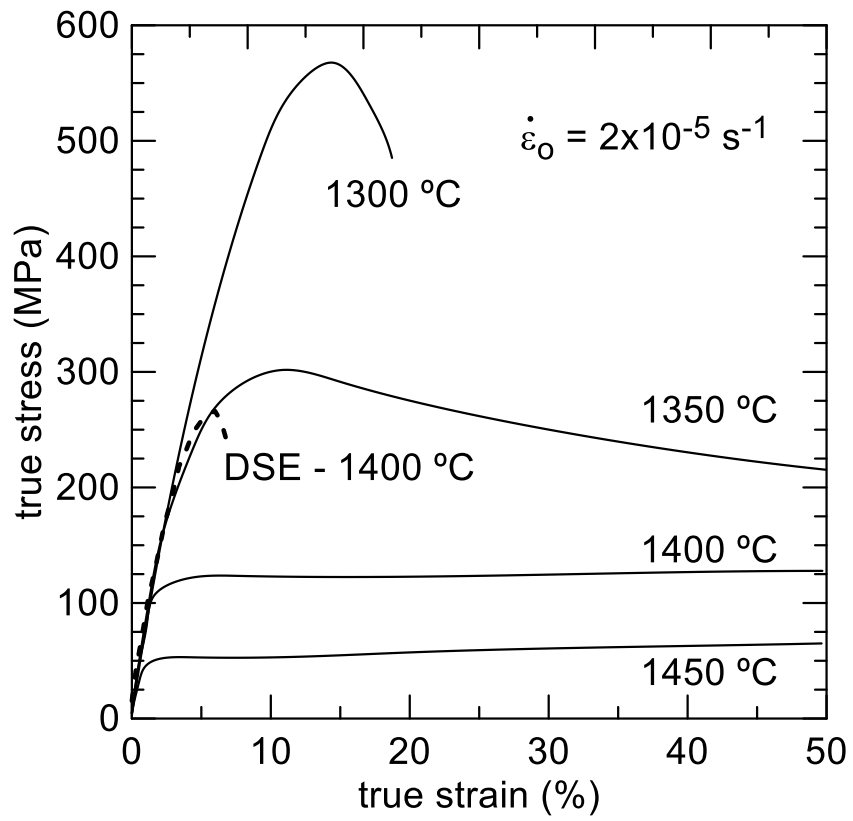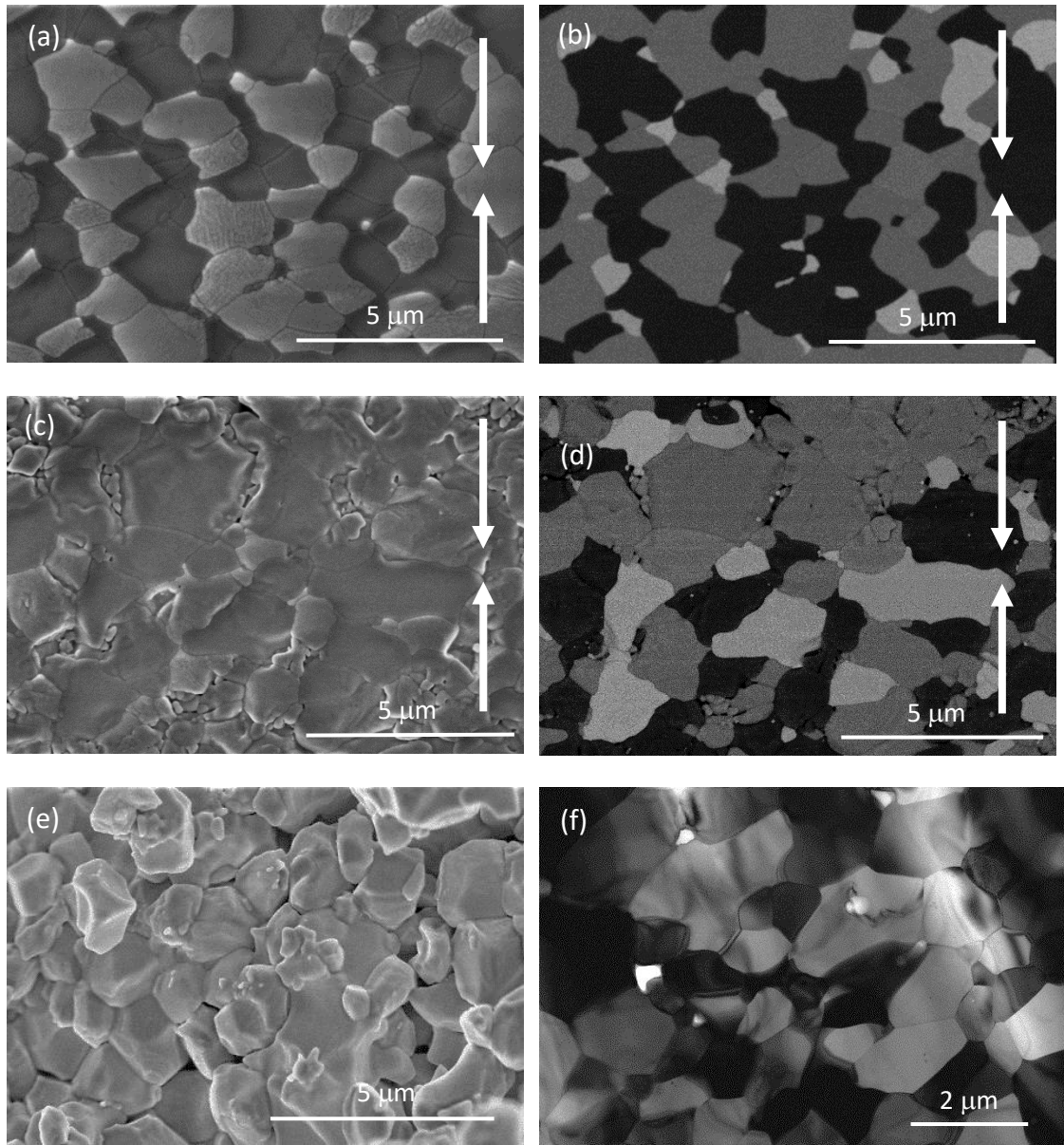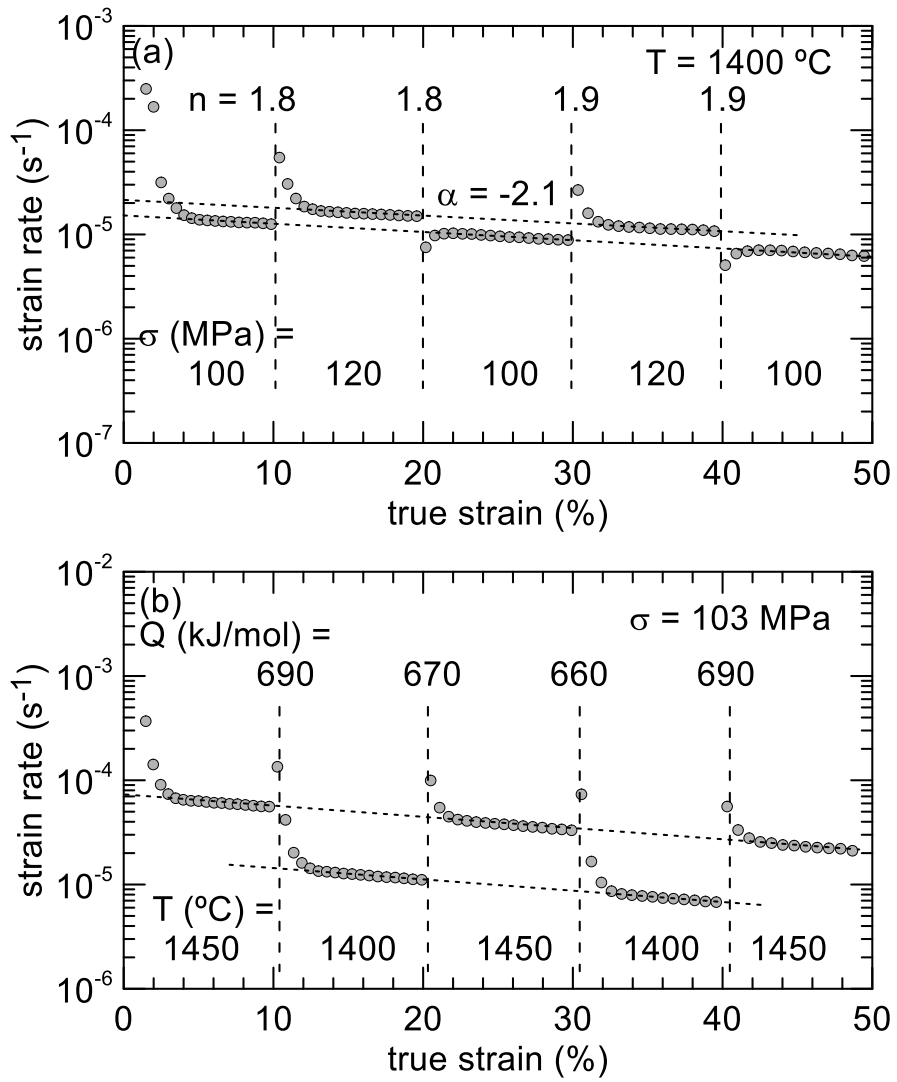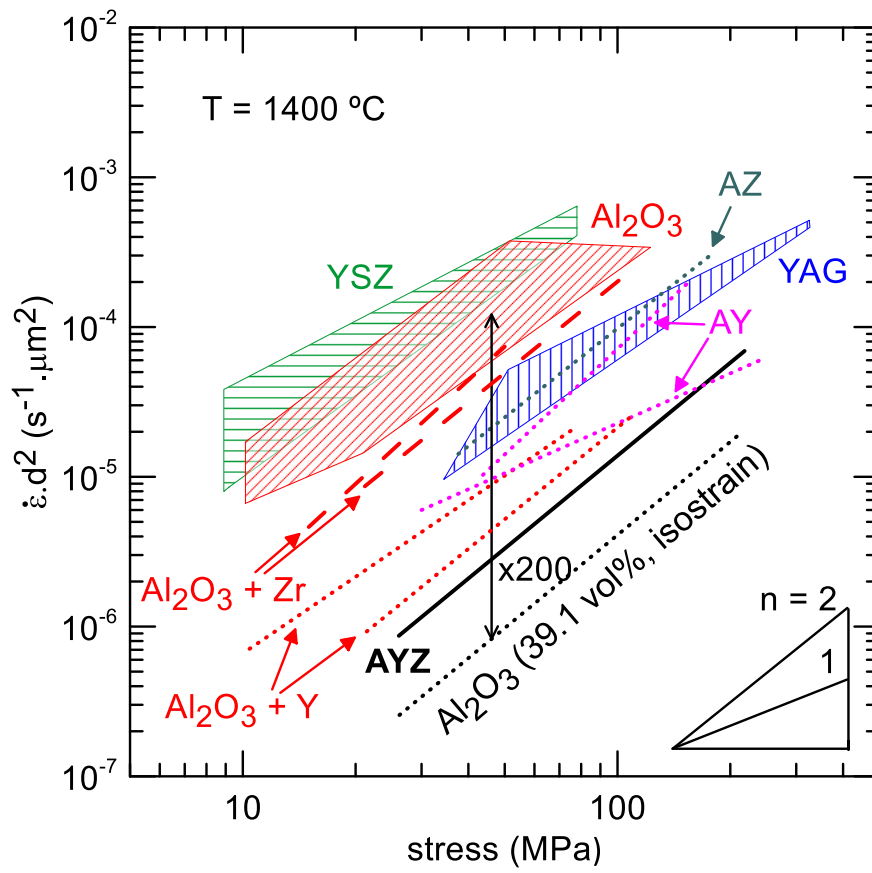
Figure 1

Figure 2

Figure 3

Figure 4

Figure 5

Figure 6

Figure 7